

Iridate Li_8IrO_6 : An Antiferromagnetic Insulator

Callista M. Skaggs, Peter E. Siegfried, Chang-Jong Kang, Craig M. Brown, Fu Chen, Lu Ma, Steven N. Ehrlich, Yan Xin, Mark Croft, Wenqian Xu, Saul H. Lapidus, Nirmal J. Ghimire, and Xiaoyan Tan*

Cite This: *Inorg. Chem.* 2021, 60, 17201–17211

Read Online

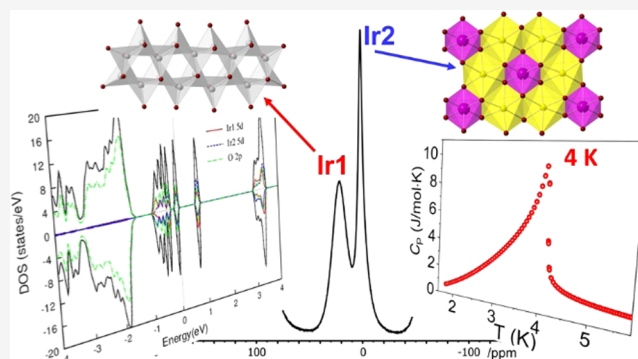
ACCESS |

Metrics & More

Article Recommendations

Supporting Information

ABSTRACT: A polycrystalline iridate Li_8IrO_6 material was prepared via heating Li_2O and IrO_2 starting materials in a sealed quartz tube at $650\text{ }^\circ\text{C}$ for 48 h. The structure was determined from Rietveld refinement of room-temperature powder neutron diffraction data. Li_8IrO_6 adopts the nonpolar space group $R\bar{3}$ with Li atoms occupying the tetrahedral and octahedral sites, which is supported by the electron diffraction and solid-state ^7Li NMR. This results in a crystal structure consisting of LiO_4 tetrahedral layers alternating with mixed IrO_6 and LiO_6 octahedral layers along the crystallographic c -axis. The +4 oxidation state of Ir^{4+} was confirmed by near-edge X-ray absorption spectroscopy. An in situ synchrotron X-ray diffraction study of Li_8IrO_6 indicates that the sample is stable up to $1000\text{ }^\circ\text{C}$ and exhibits no structural transitions. Magnetic measurements suggest long-range antiferromagnetic ordering with a Néel temperature (T_N) of 4 K, which is corroborated by heat capacity measurements. The localized effective moment $\mu_{\text{eff}}(\text{Ir}) = 1.73\ \mu_B$ and insulating character indicate that Li_8IrO_6 is a correlated insulator. First-principles calculations support the nonpolar crystal structure and reveal the insulating behavior both in paramagnetic and antiferromagnetic states.



INTRODUCTION

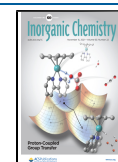
Iridates (Ir-based oxides) have drawn increasing attention because they provide a fertile playground for discovering novel electronic states and exotic physical properties, which are associated with the strong spin–orbit coupling (SOC). The large atomic number (Z) of Ir explains the strong SOC because the SOC is proportional to Z^4 .¹ Compared to 3d and 4d transition-metal oxides, iridates contain more spatially extended 5d orbitals (larger electronic bandwidth) and weaker electronic correlation, so they are expected to be less magnetic and more metallic. However, the interplay between the strong SOC, on-site Coulombic interactions (U), electronic correlations (amplified by SOC), and crystal field effect can stabilize magnetic Mott-insulating ground states with $J_{\text{eff}} = 1/2$ novel quantum states² and other exotic physical properties including correlated topological insulators³ and topological spin liquids.⁴ Moreover, applying physical pressure or chemical doping on the iridate system can drive novel interesting properties such as insulating-to-metal transition and superconductivity.^{5–7} Recent representative discoveries in iridates are non-Fermi liquid behavior in nearly ferromagnetic SrIrO_3 ,⁸ charge density wave transition in BaIrO_3 ,⁹ magnetic ordered Mott-type insulators in A_2IrO_3 ($A = \text{Li}, \text{Na}$) and Ba_2IrO_4 ,^{1,10} pressure-induced anomalous Hall effect and magnetic-field-induced multiple topological phases in pyrochlore Weyl semimetal $\text{R}_2\text{Ir}_2\text{O}_7$ ($R =$ rare-earth metal),^{11,12} metal–insulator transition in

$(\text{Sr}_{1-x}\text{La}_x)_3\text{Ir}_2\text{O}_7$,⁵ and spin-liquid ground state in hyperkagome antiferromagnetic $\text{Na}_4\text{Ir}_3\text{O}_8$.¹³

Li_8IrO_6 is a ternary iridate reported among the $A\text{--}T\text{--}O$ ($A =$ alkali or alkali-earth element, $T = \text{Ce}, \text{Pr}, \text{Pb}, \text{Tb}, \text{Zr}, \text{Hf}, \text{Sn}, \text{Pt}, \text{Ir}, \text{Ru}, \text{Co}, \text{Ge}, \text{Si}$) system.^{14–21} This study is motivated by the fact that while interesting crystal structures and physical properties are reported for many noniridium Li_8TO_6 compounds,^{17–21} the physical properties of Li_8IrO_6 are still unknown. The crystal structure of Li_8IrO_6 has been reported with a nonpolar space group $R\bar{3}$, which is isostructural to most compounds in the Li_8TO_6 ($T = \text{Ce}, \text{Pr}, \text{Pb}, \text{Tb}, \text{Zr}, \text{Hf}, \text{Sn}, \text{Pt}, \text{Ru}$) series.^{14–18} However, it is different from some other Li_8TO_6 ($T = \text{Co}, \text{Ge}, \text{Si}$) compounds adopting the polar space group ($P6_3mc$).^{19–21} The Li_8RuO_6 compound was first reported as a tetragonal or rhombohedral structure,^{14,17} but it was later determined to be Li-deficient Li_7RuO_6 in a triclinic structure (space group $P\bar{1}$), which transforms into the rhombohedral structure (space group $R\bar{3}$) at $450\text{ }^\circ\text{C}$.^{22,23}

Received: August 17, 2021

Published: November 4, 2021



Confirming the crystal structure of Li_8IrO_6 and understanding the reason for forming a nonpolar instead of a polar crystal structure will provide insights for existing and potentially novel Li_8TO_6 compounds, which hold potentials as high-capacity Li-battery cathode materials,^{24–26} solid electrolytes,²⁷ and CO_2 capture materials.²⁸ Therefore, we launched an investigation to synthesize a phase-pure sample, understand the crystal and electronic structures, and determine the physical properties of Li_8IrO_6 .

In this work, we report that almost phase-pure Li_8IrO_6 samples can be synthesized via the solid-state method in a sealed quartz tube. The crystal structure and stability are studied with neutron diffraction, in situ synchrotron X-ray diffraction, and electron diffraction experiments. We use the X-ray absorption near-edge spectroscopy (XANES) to study the oxidation state of Ir. Magnetic properties and heat capacity are measured to reveal the physical properties. Density functional theory (DFT) calculations are carried out to understand the formation of the nonpolar crystal structure and observed physical properties and the interplay between the crystal structure, electronic structure, and physical properties.

EXPERIMENTAL SECTION

Starting Materials and Synthesis. Li_8IrO_6 polycrystalline samples were synthesized using the solid-state method. Starting materials Li_2O (99.5% mass fraction, Alfa Aesar^a) and IrO_2 (99.9% mass fraction, Sigma-Aldrich) were used as received. Li_2O and IrO_2 were mixed and ground with a molar ratio of 5:1 inside an argon-filled glovebox with a low concentration of O_2 and H_2O (<1 parts per million). The thoroughly ground precursors were pressed into a pellet, which was placed in an alumina crucible, and then sealed inside a quartz tube (OD = 12.5 mm) under vacuum ($\sim 10^{-3}$ mm Hg). The ampoule was heated in a box furnace to 650 °C over 12 h and remained at the same temperature for 48 h, and then the furnace was cooled to room temperature over 6 h.

Laboratory and In Situ Synchrotron Powder X-ray Diffraction (SPXD). Powder X-ray diffraction (PXD) patterns of polycrystalline samples were collected at room temperature for 0.5 h with the scattering angle 2θ ranging from 10 to 70° using a benchtop Miniflex-600 powder X-ray diffractometer (Cu $K\alpha$, $\lambda = 1.5418$ Å). In situ synchrotron powder X-ray diffraction (SPXD) patterns were collected ($0.8 < 2\theta < 28^\circ$) in an open-end small quartz tube under argon flow at the 17-BM beamline ($\lambda = 0.45229$ Å) at the Advanced Photon Source, Argonne National Laboratory.

Powder Neutron Diffraction (PND). Powder neutron diffraction (PND) experiments were carried out at 298 K at the BT-1 beamline at the National Institute of Standards and Technology Center for Neutron Research. To minimize adsorption, about 0.5 g of the powder was loaded into a thin aluminum foil annulus and placed inside a cylindrical (6 mm diameter, 50 mm tall) vanadium cell and scanned with the 2θ range from 3 to 168° with a wavelength (λ) of 1.5400 Å. Rietveld refinements of the PND data were carried out with the suite of FullProf programs.²⁹

Transmission Electron Microscopy (TEM). The TEM experiment was performed on a probe aberration-corrected sub-angstrom resolution JEOL JEM-ARM200cF microscope with an accelerating voltage of 200 kV. Polycrystalline samples were crushed into thin electron-transparent pieces with a mortar and pestle. The crushed thin pieces were transferred onto a carbon-coated 200-mesh Cu TEM grid. Selected-area diffraction patterns and atomic resolution scanning transmission electron microscopy high-angle annular dark-field (STEM-HAADF) images were collected on a single crystal piece.

X-ray Absorption Near-Edge Spectroscopy (XANES). XANES of Li_8IrO_6 , Na_2IrO_3 , IrO_2 , and Ir samples were performed at the 7-BM beamline using a Si-111 channel-cut monochromator at the National Synchrotron Light Source II (NSLS-II), Brookhaven National Laboratory. Both transmission and fluorescent mode measurements

were made with a simultaneous standard for precision energy calibration. Standard polynomial background and post-normalization to unity were used in the analysis. Systematic comparisons to previously measured compounds were also made.

Solid-State ^7Li NMR. Polycrystalline Li_8IrO_6 was measured with a Bruker AV NEO 500 MHz solid-state NMR spectrometer with a 3.2 mm double-resonance magic-angle spinning (MAS) probe. One-dimensional (1D) ^7Li MAS NMR spectra were acquired with spinning rates of 16 and 14 kHz. Two-dimensional (2D) ^7Li multiquantum magic-angle spinning (MQMAS) NMR spectrum was also acquired at 16 kHz. The ^7Li NMR was referenced to LiCl (10 M) at 0 ppm, and the 90° pulse width in solids is 2 μs .

Thermogravimetric Analysis (TGA) and Differential Scanning Calorimetry (DSC). TGA and DSC data were collected with a PT1600 Linseis Thermal Analysis Instrument. About 20 mg of the Li_8IrO_6 polycrystalline sample was heated inside an alumina crucible from room temperature to 1273 K (held for 1 h) under argon flow with a heating/cooling rate of 10 K/min. After the measurement, the remaining sample was analyzed by PXD.

Physical Properties. Magnetic properties of Li_8IrO_6 powders were measured with the Quantum Design Physical Property Measurement System (PPMS). Field-cooled (FC) and zero-field-cooled (ZFC) magnetic susceptibility measurements were recorded between 300 and 1.8 K in direct-current applied magnetic fields of 0.1 and 1 T, respectively. Field-dependent magnetization was measured from -9 to 9 T at 1.8 and 300 K. A dense pellet (>91%) pressed at 500 °C for 4 h under 4 GPa with a Walker-type high-pressure instrument was used for electrical conductivity measurement. Heat capacity measurement was performed on a pellet between 300 and 2 K under 0 T with the PPMS.

Computational Method. Density functional theory (DFT) calculations were carried out with the all-electron full-potential linearized augmented plane-wave (FLAPW) method implemented in WIEN2k to calculate the electronic structure.³⁰ A generalized gradient approximation (GGA) functional was chosen to calculate the electronic structure. A $17 \times 17 \times 17$ k -mesh was used for the Brillouin zone integration. The muffin tin radii were chosen to be 1.59, 2.15, and 1.76 Bohr radii for Li, Ir, and O, respectively. The size of a plane-wave basis set was determined from $R_{\text{mt}}K_{\text{max}}$ of 7.0, where R_{mt} is the smallest atomic muffin tin radius and K_{max} is the largest plane-wave vector. The SOC was included in the second variational scheme. The on-site Coulombic repulsion $U = 2$ eV is considered in the Ir d orbital for the GGA + SOC + U calculations, which well explains the structure of an iridate compound.² To describe strong electronic correlation effects properly, fully charge self-consistent DFT plus dynamical mean-field theory (DFT + DMFT) were performed.^{31–33} The continuous-time quantum Monte Carlo (CTQMC) method was implemented for a local impurity solver with a proper local J effective basis.^{34,35} The fully rotational invariant form was adopted for a local Coulombic interaction Hamiltonian with on-site Coulombic repulsion $U = 4.5$ eV and $J_{\text{H}} = 0.8$ eV, where the U and J_{H} values were turned out to be valid in previous DFT + DMFT calculations on iridate compounds.^{36–38} A wide hybridization energy window from -10 to 10 eV with respect to the Fermi level was chosen. The maximum entropy method was used for analytical continuation to obtain the self-energy on the real frequency.³⁹

RESULTS AND DISCUSSION

Synthesis and Crystal Structure. The synthesis of the Li_8IrO_6 polycrystalline sample was reported by Gadzhiev using Li_2CO_3 and IrO_2 as starting materials, which were heated in air.¹⁴ Later, Hoppe prepared small Li_8IrO_6 single crystals for the first time by heating Na_2IrO_3 and Li_2O precursors in a vacuum-sealed quartz tube at 825 °C for 40 days.⁴⁰ The crystal structure of Li_8IrO_6 was solved with the nonpolar space group $R\bar{3}$ (No. 148) based on single-crystal X-ray diffraction data.⁴⁰ We first started the synthesis with Li_2CO_3 and IrO_2 in air according to the literature procedure¹⁴ but only obtained

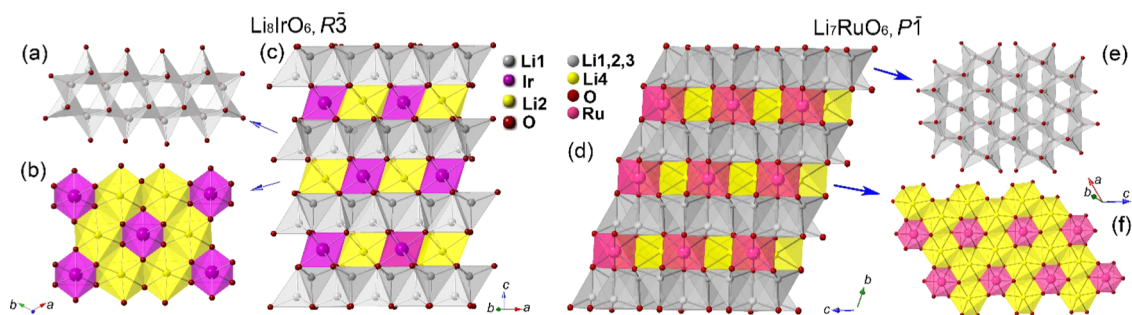


Figure 1. Crystal structures of Li_8IrO_6 with the space group $\bar{R}3$ ((a, b, c): color code: Li1/Li2 = gray/yellow, Ir = purple, O = red) and Li_7RuO_6 with the space group $P\bar{1}$ ((d, e, f): color code: Li1–3/Li4 = gray/yellow, Ru = pink, O = red).

Li_2IrO_3 as the major phase. We then modified the synthetic conditions by heating Li_2O and IrO_2 starting materials in a vacuum-sealed quartz tube and adjusting the heating profile and successfully prepared almost phase-pure Li_8IrO_6 with a small amount of Ir impurity at 650°C for 48 h according to the PXD (Figure S1) pattern. The purity of the product is dependent on the ratio of $\text{Li}_2\text{O}/\text{IrO}_2$, heating temperature, and dwell time. For the best-obtained sample, this was conducted with the optimized ratio of $\text{Li}_2\text{O}/\text{IrO}_2 = 5:1$. At lower ratios ($\text{Li}_2\text{O}/\text{IrO}_2 = 4:1$ or $4.5:1$), the Li_2IrO_3 phase is produced with no indication of the Li_8IrO_6 phase. At higher ratios ($\text{Li}_2\text{O}/\text{IrO}_2 > 5:1$), the Li_8IrO_6 phase is formed; however, there is a significant amount of unreacted Li_2O . The timing and temperature of the reaction are also critical because a higher temperature or dwell period longer than 48 h will produce the Li_2IrO_3 phase either as a significant impurity or even as the major phase.

The experimental PXD pattern matches the theoretical pattern of the reported Li_8IrO_6 with the space group $\bar{R}3$ (Figure S1). The crystal structure consists of Li_1O_4 tetrahedral layers alternating with mixed IrO_6 and Li_2O_6 octahedral layers along the crystallographic c -axis (Figure 1c). In the Li_1O_4 layer, each tetrahedron is edge-shared by three reversed Li_1O_4 tetrahedra along the crystallographic ab plane (Figure 1a). In the layer with mixed IrO_6 and Li_2O_6 , each IrO_6 octahedron is edge-shared with six Li_2O_6 octahedra, while each Li_2O_6 octahedron is only edge-shared by three Li_2O_6 octahedra (Figure 1b). The ratio of $\text{Li}_2\text{O}_6/\text{IrO}_6$ octahedra is 2:1. The IrO_6 octahedron is symmetric; however, the Li_2O_6 octahedron is distorted. The overall crystal structure is nonpolar due to the symmetric distribution of Li_2O_6 octahedra surrounding the IrO_6 octahedra. The disconnected IrO_6 octahedra in the structure are different from the honeycomb layers of IrO_6 observed in A_2IrO_3 ($A = \text{Li}, \text{Na}, \text{Cu}$)^{41,42} but were observed in the related compounds Li_7MO_6 ($M = \text{Ru}, \text{Nb}, \text{Ta}, \text{Sb}, \text{Bi}, \text{Os}$) with the space group $P\bar{1}$.^{22,23,43} In the crystal structure of Li_7RuO_6 , there are four Li sites and the occupancy for each site is 0.875. Similar to Li_8IrO_6 , the crystal structure of Li_7RuO_6 (Figure 1d) consists of layers of edge-shared Li_4O_6 and RuO_6 octahedra (Figure 1f), which alternate with the layers constructed by Li_1O_4 , Li_2O_4 , and Li_3O_4 tetrahedra (Figure 1e).

To accurately refine the crystal structure of the prepared Li_8IrO_6 sample, a PND experiment was carried out at room temperature. The reported structure was used as the starting model for Rietveld refinement, and the PND pattern (Figure 2) can be refined with the major phase Li_8IrO_6 (mass % = 96.1%), a small amount of impurity Li_2O (mass % = 3.9%), and a small unidentified peak near 42° . The detected small

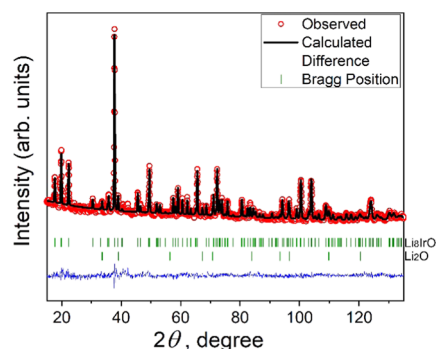


Figure 2. Rietveld refinement of PND (298 K) of Li_8IrO_6 ($\bar{R}3$ space group, $\lambda = 1.5400 \text{ \AA}$) with observed data (red), calculated pattern (black), Bragg peak position (green), and the difference between the observed and calculated patterns (blue).

amount of impurity in the PND is different from PXD because the former is more sensitive to light elements and has strong absorption for Ir and Li. Selected refined structural parameters and bond distances are given in Tables 1, 2, and S1. The refined lattice parameters using PND data are $a = b = 5.40920(8) \text{ \AA}$, $c = 15.0401(3) \text{ \AA}$, and $V = 381.10(1) \text{ \AA}^3$, which are close to the reported values $a = b = 5.4151(6) \text{ \AA}$, $c = 15.058(4) \text{ \AA}$, and $V = 382.4(1) \text{ \AA}^3$.⁴⁰ In the refined structure, Li1, Li2, Ir, and O atoms occupy the 18f (0.629, 0.647, 0.8816), 6c (0, 0, 0.3396), 3a (0, 0, 0), and 18f (0.6765, 0.6474, 0.4122) sites, respectively. These values are also close to the previously reported ones.

As shown in Figure 1, each IrO_6 octahedron is symmetric, and the refined Ir–O bond distance is $2.049(3) \text{ \AA}$, which is within the range of reported Ir–O bond distances ($1.97\text{--}2.08 \text{ \AA}$) in Li_2IrO_3 .⁴⁴ In the distorted Li_1O_4 tetrahedron, three different Li–O bond distances are $1.89(1)$, $1.96(1)$, and $2.045(7) \text{ \AA}$ (Table 2). The distorted Li_2O_6 octahedron only contains two unequal bond distances, $2.113(8) \text{ \AA}$ and $2.327(8) \text{ \AA}$. The Li–O bond distances are close to these ($1.88\text{--}2.34 \text{ \AA}$) in Li_2IrO_3 as well. The closest Ir–Li and Li–Li distances are also shown in Table 2. Based on the Ir–O bond distances, the bond valence sum of Ir was calculated to be 4.1,⁴⁵ indicating an oxidation state of +4. During the refinement, the overall fitting was not improved when the occupancies of Li or O sites were initially refined with about 5% vacancies. Therefore, the site's occupancies were set at unity in the later stages of the refinement considering the charge-balanced Ir^{4+} confirmed by XANES and extra Li_2O observed in the sample as well.

Electron Diffraction. To gain further insight into the crystal structure of Li_8IrO_6 , a TEM experiment was carried out on thin pieces of polycrystalline samples. Figure 3a shows the

Table 1. Selected Structural Parameters of Rietveld Refinement of PND Data of Li_8IrO_6 ^b

sample	Li_8IrO_6		
empirical formula	Li_8IrO_6		
temperature	298 K		
mol. wt., g/mol	343.74		
density (calculated), g/cm ³	4.493		
neutron wavelength, λ	1.5400 Å		
space group, #	$R\bar{3}$, #148		
Z	3		
lattice parameters	$a = b = 5.40920(8)$ Å, $c = 15.0401(3)$ Å, $V = 381.10(1)$ Å ³ , $\alpha = \beta = 90^\circ$, $\gamma = 120^\circ$		
Rietveld criteria of fit ^a	$R_p = 3.86\%$, $R_{wp} = 4.77\%$, $R_{exp} = 4.53\%$, $\chi^2 = 1.11$		
site	Wyckoff symbol	x, y, z	occ.
Li1	18f	0.629(2), 0.647(2), 0.8816(4)	1
Li2	6c	0, 0, 0.3396(9)	1
Ir	3a	0, 0, 0	1
O	18f	0.6765(6), 0.6474(6), 0.4122(2)	1

^a $R_{wp} = \sqrt{\frac{\sum_i w_i (y_i^{\text{calcd}} - y_i^{\text{obs}})^2}{\sum_i w_i (y_i^{\text{obs}})^2}}$, $R_{exp} = \sqrt{\frac{N-P}{\sum_i w_i (y_i^{\text{obs}})^2}}$, $R_p = \sqrt{\frac{\sum_i (y_i^{\text{calcd}} - y_i^{\text{obs}})^2}{\sum_i (y_i^{\text{obs}})^2}}$, $\chi^2 = (R_{wp}/R_{exp})^2$, where y_i^{calcd} and y_i^{obs} are the calculated and observed intensities at the i th data point, respectively, the weight w_i is $1/\sigma^2$ from counting statistics, with the same normalization factor, N is the number of measured data points, and P represents the number of refined parameters. ^bValues in parentheses indicate 1σ .

Table 2. Selected Bond Distances in Li_8IrO_6 ^a

	Ir–O/Li distances (Å)		Li–O distances (Å)		Li–Li distances (Å)
Ir–O	$2.049(3) \times 6$	Li1–O	$1.89(1) \times 2$	Li1–Li1	2.34(1)
Ir–Li1	2.646(1)	Li1–O	$1.96(1) \times 1$	Li1–Li1	2.88(1)
Ir–Li2	3.216(1)	Li1–O	$2.045(7) \times 1$	Li1–Li2	2.46(1)
		Li2–O	$2.113(8) \times 3$	Li1–Li2	2.52(1)
		Li2–O	$2.327(8) \times 3$		

^aValues in parentheses indicate 1σ .

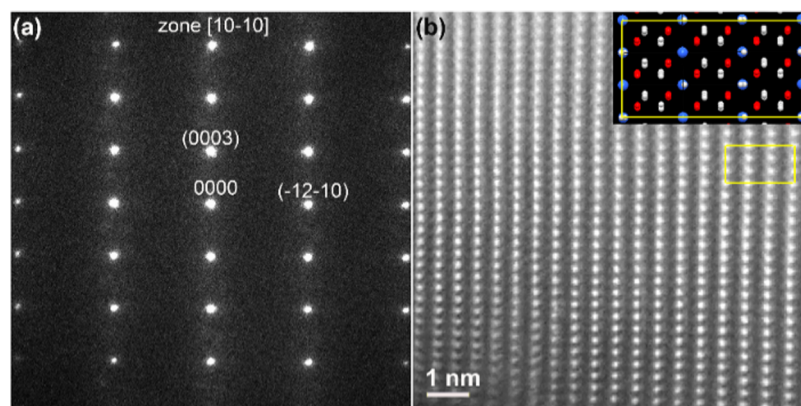


Figure 3. (a) Electron diffraction pattern recorded along the $[10\bar{1}0]$ direction and (b) corresponding STEM-HAADF image. Inset shows the projected atomic structure with Ir atoms in blue, O atoms in red, and Li atoms in white.

electron diffraction obtained along the $[10\bar{1}0]$ direction. The indexed (0000), (0003), and $(\bar{1}210)$ planes obey the refined structure with the $R\bar{3}$ space group. The STEM-HAADF image recorded along the $[10\bar{1}0]$ direction is shown in Figure 3b with the schematic projected atomic structure as an inset. The white dots are projected atomic columns. The intensity of a dot is directly related to the atomic number (Z) of the atom and the numbers of atoms in each column, and the higher Z columns show higher intensity. The white dots in Figure 3b are the atomic columns consisting of Ir and Li atoms, which correspond to the edge-sharing IrO_6 and Li_2O_6 and octahedral mixed layer. The distance between the Ir/Li column is 4.74 Å. The O and Li columns, which correspond to the LiIO_4

tetrahedral layers in between, have too low Z numbers compared with Ir to have enough intensity to be clearly visible in the image.

In Situ Synchrotron Powder X-ray Diffraction. Because the Li_2IrO_3 phase is frequently identified as a major phase or impurity under different synthetic conditions and a structural transition is observed in the related Li_2MO_6 ($T = \text{Bi, Ru, Os}$) series,²² we carried out a TGA–DSC experiment to check the stability of Li_8IrO_6 . The TGA–DSC experiment was carried out under argon flow (10 K/min heating rate), and the sample was heated to 1273 K and retained at the same temperature for 1 h. A PXD of the sample after the TGA–DSC measurement shows that it still remains the same Li_8IrO_6 phase (Figure S1).

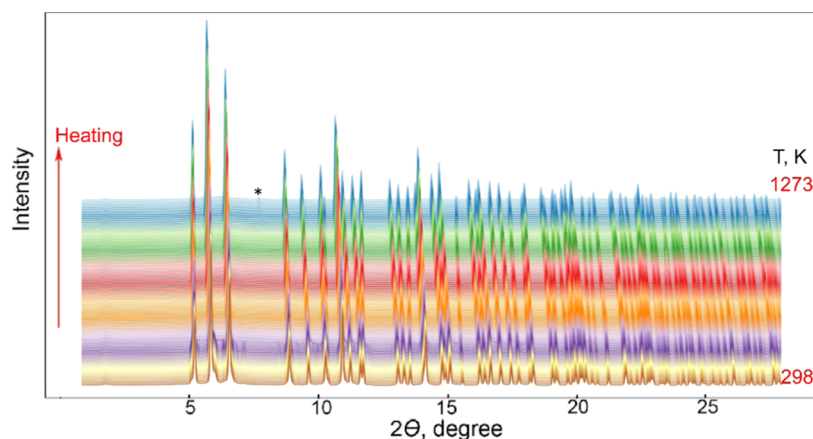


Figure 4. In situ SPXD patterns of Li_8IrO_6 obtained while heating from 298 to 1273 K ($\lambda = 0.45229 \text{ \AA}$, the SiO_2 peak is marked with an asterisk *).

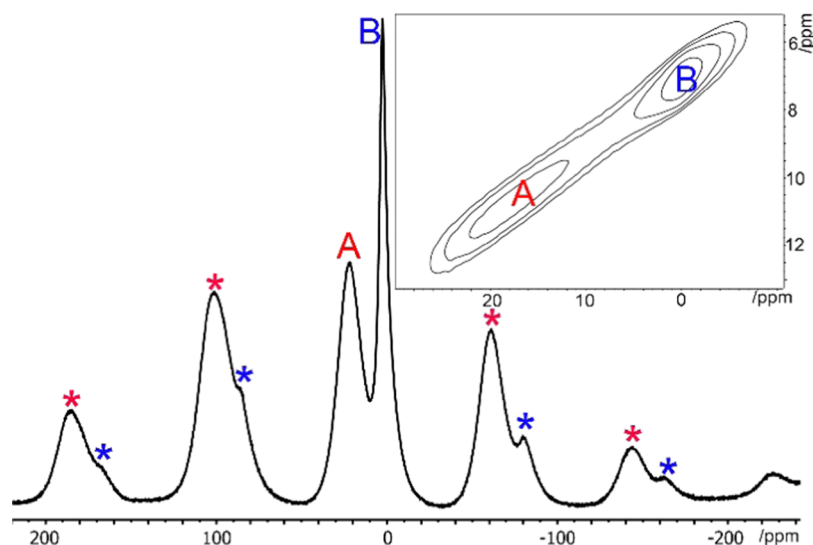


Figure 5. One-dimensional (1D) solid-state ^7Li MAS spectrum with 2D ^7Li MQMAS NMR as inset.

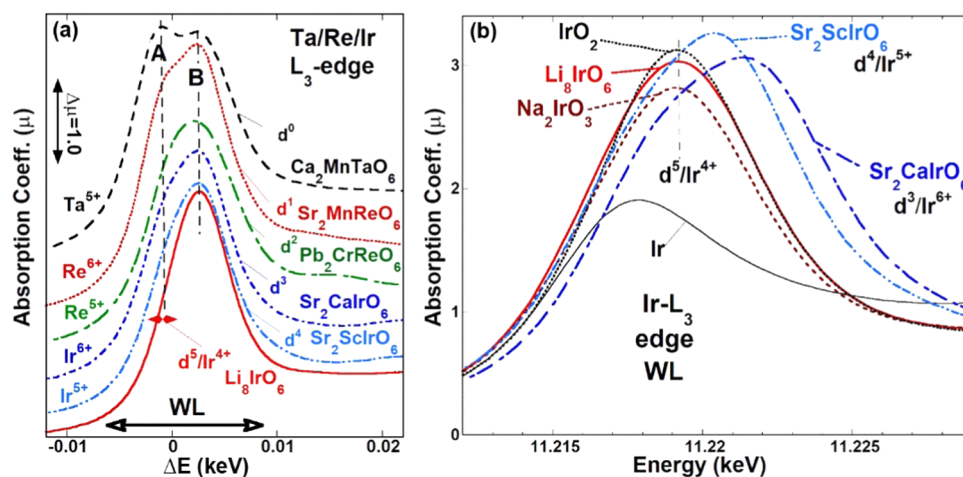


Figure 6. (a) $T_{5d}\text{-}L_3$ near edges of Li_8IrO_6 and a series of standard octahedral $T_{5d}\text{-}O$ compounds with spectra shifted in energy to approximately align the B-features with the zero of the relative energy scale being arbitrary. (b) Calibrated energy Ir-L_3 near edges for a series of standard Ir materials.

The mass of the sample remains practically constant during the experiment, and the DSC curve shows a small exothermic peak at 689 K (Figure S2).

To further monitor the stability of Li_8IrO_6 and study a possible structural change from Li_8IrO_6 , we carried out the in situ SPXD by heating the sample under argon flow from 298 to 1273 K at a 10 K/min heating rate and cooling to room

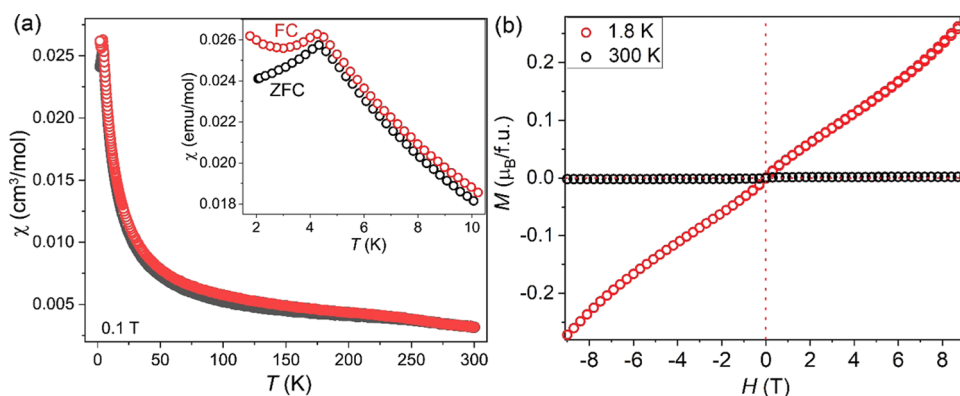


Figure 7. (a) FC–ZFC magnetic susceptibility of Li_8IrO_6 with an applied magnetic field of 0.1 T (inset shows the zoomed low-temperature range). (b) Field-dependent magnetization measured at 1.8 and 300 K between -9 and 9 T.

temperature at a 50 K/min rate. As shown in Figure 4, the Li_8IrO_6 phase remains intact as the temperature increases, and a small new Bragg peak near 7.7° shows up at high temperatures, which is identified as SiO_2 that results from the partial crystallization of the fused quartz of the sample tube. When the temperature is cooled from 1273 K, the Li_8IrO_6 phase and SiO_2 impurity remain (Figure S3). It appears that Li_8IrO_6 is stable during the in situ experiment, which is in contrast to the triclinic (space group $P1$) to rhombohedral (space group $R\bar{3}$) structural transition observed in related compounds Li_xMO_6 ($M = \text{Bi}, \text{Ru}, \text{Os}$).²²

Solid-State ^7Li NMR. To confirm the two Li sites with different coordinates in the structure, solid-state NMR experiments were carried out. 1D solid-state ^7Li MAS (Figure 5) and 2D ^7Li MQMAS NMR spectra acquired at 16 kHz (inset of Figure 5) clearly indicate there are two Li sites (labeled as A and B) in the polycrystalline Li_8IrO_6 sample. The chemical shifts of peaks A and B are 22.2 ppm and 2.7 ppm, respectively. The peaks labeled with asterisks in Figure 5 are spinning sidebands for A and B sites. It is clear that peak A has a relatively larger ^7Li quadrupolar coupling constant than peak B due to the larger linewidth of peak A. As discussed in related Li_xMO_6 ($M = \text{Nb}, \text{Ta}, \text{Sb}, \text{Bi}$) compounds,^{43,46} Li atoms with tetrahedral coordination are more deshielded than Li atoms with octahedral coordination. It is also reasonable that the symmetry of the Li atom in a tetrahedral environment is not as high as in an octahedral environment. Thus, peaks A and B are signals corresponding to Li1 atoms in Li1O_4 tetrahedra and Li2 atoms in Li2O_6 octahedra.

X-ray Absorption Near-Edge Spectroscopy (XANES). Based on the structural refinement in the nominal composition of Li_8IrO_6 and bond valence sum of Ir (4.1), the oxidation state of Ir is expected to be +4. XANES experiments were carried out using the Li_8IrO_6 polycrystalline powder with Li_2IrO_3 , IrO_2 , and Ir as standard materials. The obtained Ir- L_3 near-edge spectra were also compared with a series of standard 5d transition-metal (T_{5d}) oxides, which manifest intense atomic-like p to d transitions, the so-called “white line” (WL) features, as illustrated in Figure 6a. Both the spectral shape and the chemical shift of the T_{5d} L_3 edges offer insight into the d-configuration/valence.^{47–54}

The L_3 -edge spectral shape in T_{5d} oxides is dominated by the octahedral ligand field splitting of the 5d orbitals into lower-lying 6X degenerate t_{2g} and higher energy 4X degenerate e_g orbital states. The dashed lines emphasize the bimodal WL, $A(t_{2g} \text{ hole})/B(e_g \text{ hole})$ related features typical of such

compounds. As shown in Figure 6a, transitions into these split t_{2g}/e_g final-hole states can be seen to yield a bimodal A/B WL feature in the 5d- L_3 edge spectra. The A- and B-feature intensities are, respectively, related to the number of available t_{2g} and e_g final states (hole count) weighted by transition matrix element effects. In the compounds considered in Figure 6a, the e_g hole count (and the B-feature intensity) remains essentially constant. On the other hand, the intensity of the A-feature (relative to that of the B-feature) very dramatically decreases as the t_{2g} hole count decreases from 6 in d^0/Ta^{5+} - $\text{Ca}_2\text{MnTaO}_6$ to 2 in d^4/Ir^{5+} - $\text{Sr}_2\text{ScIrO}_6$. Thus, the relative A/B-feature intensities provide direct insight into the T_{5d} d-configuration/valence. The Li_8IrO_6 spectrum manifests an A-feature intensity (red-double-headed-arrow energy range) that is substantially reduced with respect to that of the d^4/Ir^{5+} - $\text{Sr}_2\text{ScIrO}_6$ spectrum. This substantial reduction supports the assignment of the d^5/Ir^{4+} configuration for Li_8IrO_6 .

In Figure 6b, the calibrated energy Ir- L_3 near edges of Li_8IrO_6 are compared with a series of standard iridates. The expanded scale for the Ir- L_3 spectra underscores the much stronger shoulder, A-feature intensity in the d^4/Ir^{5+} - $\text{Sr}_2\text{ScIrO}_6$ and d^3/Ir^{6+} - $\text{Sr}_2\text{CaIrO}_6$ spectra, compared to the d^5/Ir^{4+} - IrO_2 , Na_2IrO_3 , and Li_8IrO_6 spectra. Additionally, the strong chemical shift to higher energy with increasing Ir valence can be seen in the spectra. The very low and close coincidence of the chemical shifts are observed in the IrO_2 , Na_2IrO_3 , and Li_8IrO_6 spectra due to their common d^5/Ir^{4+} configuration. Thus, the d^5/Ir^{4+} configuration in Li_8IrO_6 is strongly supported by both the spectral shape and chemical shift of its Ir- L_3 spectrum.

Magnetic Properties and Heat Capacity. Field-cooled (FC) and zero-field-cooled (ZFC) temperature-dependent magnetic susceptibility was measured on Li_8IrO_6 samples with applied magnetic fields of 0.1 and 1 T. The antiferromagnetic ordering is observed below 4 K, as shown in the inset of Figure 7a. The FC–ZFC data measured at 0.1 T are almost overlapping in the temperature range from 300 to 4 K. A similar antiferromagnetic (AFM) ordering temperature has also been observed in related Li_7RuO_6 ($T_N = 6.5, 12$ K) and Li_7OsO_6 ($T_N = 13$ K) compounds in which RuO_6 and OsO_6 octahedra are also disconnected in the structure.^{22,55} The isothermal field dependences of magnetization were measured at 1.8 and 300 K, with the magnetic field varying from -9 to 9 T (Figure 7b). The nearly linear feature of magnetization measured at 1.8 K supports the AFM transition in the system.

Because of the very small magnetic moment at a high temperature and small external magnetic fields, the FC–ZFC

data measured at 0.1 T deviate from the Curie–Weiss behavior. The Curie–Weiss behavior is evident in the data collected at 1 T above 170 K as shown in Figure S4. Fitting the FC magnetic susceptibility data between 170 and 300 K with the Curie–Weiss equation $\chi = \chi_0 + C/(T - \Theta_w)$ yields the constant diamagnetic term $\chi_0 = -1.7 \times 10^{-4} \text{ cm}^3/\text{mol}$, effective magnetic moment ($\mu_{\text{eff}} = 1.73 \mu_B/\text{f.u.}$) given by $\sqrt{8C}$, where C is the Curie constant, and Weiss temperature Θ_w to be -92 K . The negative Θ_w value obtained is consistent with the presence of the AFM interaction and gives a rather large frustration factor $f = 23$. The μ_{eff} value is the same as the theoretical value $1.73 \mu_B$ for typical $S = 1/2$ of Ir^{4+} in the low spin state (t_{2g}^5) with the large crystal field splitting effect in IrO_6 octahedra. This exact μ_{eff} value is rather fortuitous and may depend slightly on the χ_0 as there are three parameters in the fitting equations. But it clearly suggests the $S = 1/2$ state of Ir^{4+} ion. An $S = 1/2$ has been reported in the honeycomb lattice material A_2IrO_3 ($A = \text{Li, Na, Cu}$),^{41,42} and frustrated hyperkagome antiferromagnet $\text{Na}_4\text{Ir}_3\text{O}_8$.¹³ In some other Ir^{4+} compounds, such as Sr_2IrO_4 ($0.2\text{--}0.5 \mu_B/\text{Ir}$),^{2,56} Ba_2IrO_4 ($0.34 \mu_B/\text{Ir}$),⁵⁷ $\text{Y}_2\text{Ir}_2\text{O}_7$ ($\sim 0.5 \mu_B/\text{Ir}$),⁵⁸ and $\text{Sr}_3\text{Ir}_2\text{O}_7$ ($\sim 0.5 \mu_B/\text{Ir}$),⁵⁹ the proposed mechanism suggests that strong spin–orbit coupling and electron correlation cause the t_{2g} orbit split into novel $J_{\text{eff}} = 1/2$ and $3/2$ orbitals, and the one unpaired electron occupies the novel $J_{\text{eff}} = 1/2$ quantum state. Whether or not Li_8IrO_6 also forms the novel $J_{\text{eff}} = 1/2$ quantum state requires further measurements such as polarization and angular dependence of XAS, resonant inelastic X-ray scattering (RIXS), angle-resolved RIXS, X-ray resonant magnetic diffraction (XRMS), and angle-resolved photoemission spectroscopy (ARPES) measurements. To reveal the magnetic structure and magnetic moment of Ir^{4+} , neutron diffraction experiments will be carried out at 1.8 K in the future.

The temperature-dependent heat capacity (C_p) measurement conducted on a pellet exhibits a λ -like anomaly at 4 K (Figure 8), which confirms the long-range AFM ordering

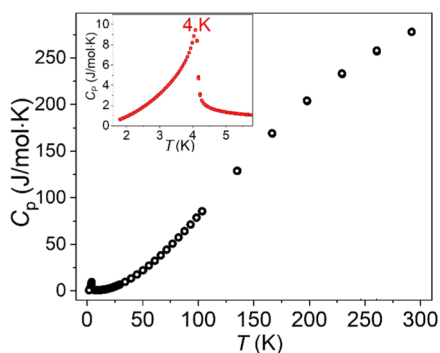


Figure 8. Heat capacity of Li_8IrO_6 measured from 1.8 to 300 K under 0 T. Left upper inset shows an enlarged curve between 1.8 and 6 K.

occurring at 4 K. A resistivity measurement was attempted on a dense pellet (density > 91%) but the high sample resistivity and the power limits of the excitation source prevented measuring the sample resistivity via the standard PPMS resistivity option. Ionic conductivity measurements were not carried out on this material but ionic conductivity is observed in Li_8TO_6 ($T = \text{Ce, Zr, Hf, Sn}$) and Li_7MO_6 ($M = \text{Nb, Bi, Ru, Os}$) above 300 °C.^{22,27} The insulating behavior and magnetic ordering have been observed in A_2IrO_3 ($A = \text{Li, Na, Cu}$),⁶⁰ doped BaIrO_3 ,⁶¹ CaIrO_3 ,⁶² Sr_2IrO_4 ,² and the spin-liquid state

of $\text{Na}_4\text{Ir}_3\text{O}_8$,¹³ which are magnetically ordered Mott-type insulators.

Electronic Structure Calculations. To understand the electronic structure and nature of the insulating behavior, DFT calculations were performed. First, the nonmagnetic (NM) electronic structure calculations were carried out with DFT relaxed lattice parameters ($a = b = 5.4344 \text{ \AA}$, $c = 15.0959 \text{ \AA}$) similar to the experimental values ($a = b = 5.4092 \text{ \AA}$, $c = 15.0401 \text{ \AA}$) of Li_8IrO_6 with the space group $R\bar{3}$. Figure 9 shows

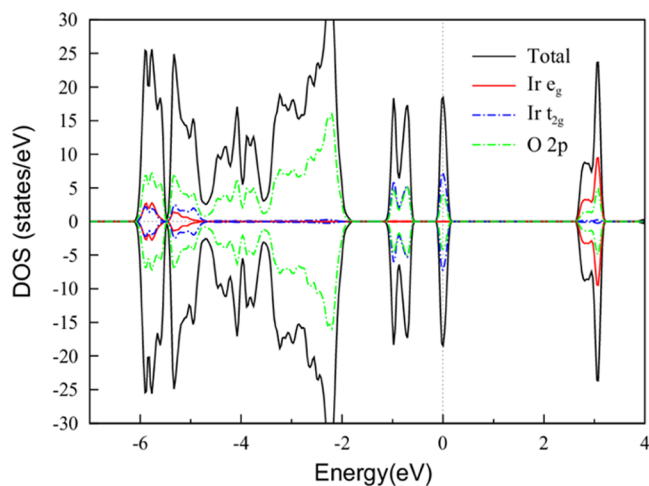


Figure 9. DOS of the NM phase with the DFT GGA + SOC + U ($=2 \text{ eV}$) method.

the electronic density of states (DOS) of the NM phase with the GGA + SOC + U (2 eV) method, which demonstrates nonzero DOS at the Fermi level, thereby showing a metallic state. The metallic state remains when the U is increased to 4 eV (Figure S5) within the DFT framework. This is in contrast to the experimental insulating behavior. Since DFT underestimates electronic correlations, more advanced methods are necessary. This issue could be resolved using DFT + DMFT, which will be discussed later.

Because related Li_8TO_6 ($T = \text{Co, Ge, Si}$) compounds adopt the polar space group ($P6_3mc$), we also calculated the NM electronic structure of hypothetical Li_8IrO_6 with DFT relaxed lattice parameters ($a = b = 5.5946 \text{ \AA}$, $c = 10.8621 \text{ \AA}$) based on the reported crystal structure information of Li_8CoO_6 with the space group $P6_3mc$. The results indicate that there is a small band gap (0.277 eV), and the required energy of the hypothetical hexagonal Li_8IrO_6 structure (space group $P6_3mc$) is +1.96 eV/f.u., which is much larger than that (+0.164 eV/f.u.) of Li_8IrO_6 in the rhombohedral structure (space group $R\bar{3}$) as shown in Table 3. The hypothetical hexagonal structure (space group $P6_3mc$) contains IrO_4 tetrahedra with an Ir coordination number of 4, which is

Table 3. Summary of DFT Calculations of Different Models and Crystal Structures of Li_8IrO_6 ^a

	$R\bar{3}$ AFM	$R\bar{3}$ FM	$R\bar{3}$ NM	$P6_3mc$ NM
energy (eV/f.u.)	0	+0.001	+0.164	+1.96
$\mu(\text{Ir})$ spin (μ_B)	0.23	0.24	0	0
band gap (eV)	0.674	0.598	0	0.277

^aThe model with the $R\bar{3}$ space group with AFM ordering is chosen as the reference energy.

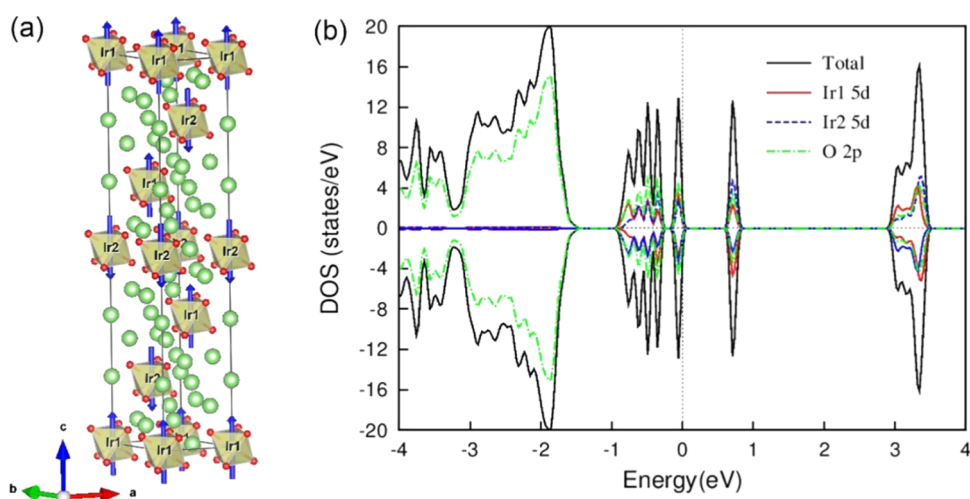


Figure 10. AFM model and the corresponding DOS with the DFT GGA + SOC + U ($=2$ eV) method.

smaller than that (6) in the rhombohedral structure ($R\bar{3}$). When the Madelung energy is computed for both structures, IrO_6 in the nonpolar space group $R\bar{3}$ is much more stable than the IrO_4 in the polar space group $P6_3mc$ because a higher coordinate number of Ir atoms reduces the Coulombic potential energy. This explains why the Li_8IrO_6 adopts the nonpolar space group $R\bar{3}$ instead of the polar space group $P6_3mc$. In the reported Li_8TO_6 ($T = \text{Ce, Pr, Pb, Tb, Zr, Hf, Sn, Pt, Ir, Ru, Co, Ge, Si}$) compounds (Table S2), those with the radius (r) of T^{4+} ($r(\text{Co}^{4+}) = r(\text{Ge}^{4+}) = 0.53 \text{ \AA}$, $r(\text{Si}^{4+}) = 0.4 \text{ \AA}$) smaller than that (0.625 \AA) of Ir^{4+} adopt the hexagonal structure, while those with $r(\text{T}^{4+}) \geq 0.625 \text{ \AA}$ crystallize in the rhombohedral structure. It is reasonable that larger T^{4+} cations can coordinate with six oxygen anions in the rhombohedral structure, while smaller T^{4+} cations coordinate with four oxygen anions in the hexagonal structure. Following this trend, Li_8IrO_6 with $r(\text{Ir}^{4+}) = 0.625 \text{ \AA}$ is expected to adopt the space group of $R\bar{3}$.

To further understand the magnetic properties and nature of the insulating feature, we carried out GGA + SOC + U calculations with an AFM model as shown in Figure 10. The computational results shown in Table 3 indicate that the AFM model has the lowest energy among the other magnetic solutions. Therefore, AFM ordering is the ground state, which confirms the experimental long-range AFM magnetic behavior. It is worth noting that many different AFM models are available, and the ground-state AFM state is not unambiguously determined yet. The details of the electronic structure of the ground-state AFM might change; however, it does not alter the general conclusion of this study. Ir-5d and O p orbitals contribute to the DOS near the Fermi level mainly and they are highly hybridized with each other (Figure 10b). It suggests that the covalent bonding between Ir and O atoms is the main bonding character to explain physical and chemical properties of this system. The AFM and ferromagnetic (FM) models have band gaps of 0.674 and 0.598 eV, respectively, which indicates that magnetic ordering results in an insulating gap for Li_8IrO_6 . Electron occupancy in Ir d orbitals is 5.47, which is away from an integer value due to the large hybridization between Ir d and O p orbitals (Figure 10). The spin and orbital moments of Ir are 0.23 μ_B/Ir and 0.40 μ_B/Ir , respectively, and the total moment is 0.63 μ_B/Ir , which is much smaller than the theoretical values of Ir^{4+} ion with $S = 1/2$. To capture the strong electronic

correlation effects presented in this compound, DFT + DMFT calculations were performed. Figure 11 shows the DOS of the

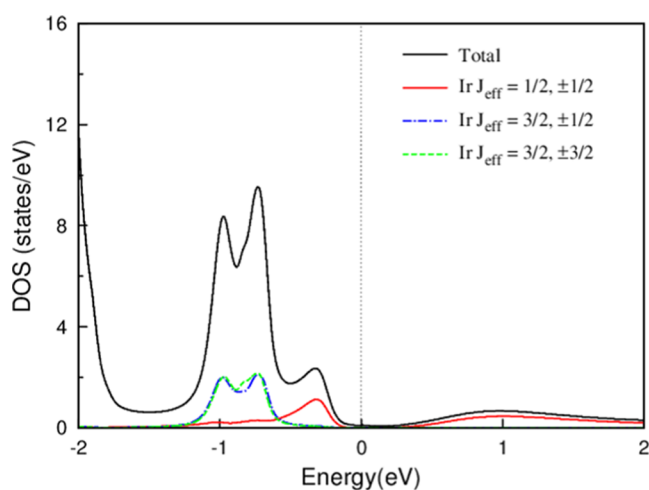


Figure 11. DOS of the NM phase computed by the DFT + DMFT method at $T = 116 \text{ K}$. Orbital-resolved Ir effective J DOS is provided.

NM phase computed by DFT + DMFT at $T = 116 \text{ K}$, which is well above the long-range antiferromagnetic ordering temperature (4 K). It demonstrates the finite band gap of $\sim 0.3 \text{ eV}$ even at a high temperature. It is noteworthy that DFT does not open the band gap in the NM phase, while DFT + DMFT does. Therefore, dynamic correlations are more important than static ones in opening the band gap in the NM phase. The DFT + DMFT results explain the insulating behavior well above T_N as observed in the experimental measurements. It indicates that this compound is a correlated insulator like other iridate compounds.^{63,64}

CONCLUSIONS

We prepared almost phase-pure Li_8IrO_6 polycrystalline materials using a solid-state method. The crystal structure was confirmed with Rietveld refinement based on powder neutron diffraction data, solid-state ^7Li NMR, and electron diffraction. In situ synchrotron X-ray diffraction data collected from room temperature to 1000 $^\circ\text{C}$ indicates the sample is stable at a high temperature under an inert atmosphere.

Magnetic properties indicate that Li_8IrO_6 orders antiferromagnetically at 4 K, which is confirmed by the heat capacity measurements. The oxidation state of Ir^{4+} is supported by the structural refinement and XANES measurement and is consistent with the result obtained from Curie–Weiss fit to the high-temperature susceptibility. Resistivity measurement attempts suggest that Li_8IrO_6 is an insulator, and DFT and DFT + DMFT calculations support the insulating behavior. A powder neutron diffraction experiment will be carried out at low temperatures to determine the magnetic structure in the near future. Li_8IrO_6 is the first example of A_8TO_6 ($\text{A} = \text{Li}, \text{Na}$; $\text{T} =$ transition metal) compounds in which we studied the physical properties. Our results thus provide a foundation to study other A_8TO_6 compounds as the magnetic and transport properties can be further modified by substituting Ir^{4+} with other T^{4+} in novel $\text{A}_8\text{Ir}_{1-x}\text{T}_x\text{O}_6$ ($\text{A} = \text{Li}, \text{Na}$; $\text{T} =$ transition metal; $0 < x < 1$) compounds.

■ ASSOCIATED CONTENT

SI Supporting Information

The Supporting Information is available free of charge at <https://pubs.acs.org/doi/10.1021/acs.inorgchem.1c02535>.

PXD patterns of experimental Li_8IrO_6 and after DSC measurement; TGA–DSC curves; refined structural parameters of the Li_2O phase; in situ SPXD patterns of Li_8IrO_6 while cooling; inverse FC magnetic susceptibility; and summary of Li_8TO_6 compounds (PDF)

■ AUTHOR INFORMATION

Corresponding Author

Xiaoyan Tan – Department of Chemistry and Biochemistry, George Mason University, Fairfax, Virginia 22030, United States; orcid.org/0000-0002-1742-8252; Email: xtan6@gmu.edu

Authors

Callista M. Skaggs – Department of Chemistry and Biochemistry, George Mason University, Fairfax, Virginia 22030, United States

Peter E. Siegfried – Department of Physics and Astronomy and Quantum Science and Engineering Center, George Mason University, Fairfax, Virginia 22030, United States; orcid.org/0000-0002-0145-2899

Chang-Jong Kang – Department of Physics, Chungnam National University, Daejeon 34134, Republic of Korea; orcid.org/0000-0003-2895-4888

Craig M. Brown – National Institute of Standards and Technology, Gaithersburg, Maryland 20899, United States; orcid.org/0000-0002-9637-9355

Fu Chen – Department of Chemistry and Biochemistry, University of Maryland, College Park, Maryland 20742, United States

Lu Ma – NSLS-II, Brookhaven National Laboratory, Upton, New York 11973, United States

Steven N. Ehrlich – NSLS-II, Brookhaven National Laboratory, Upton, New York 11973, United States

Yan Xin – National High Magnetic Field Laboratory, Tallahassee, Florida 32310, United States

Mark Croft – Department of Physics and Astronomy, Rutgers, The State University of New Jersey, Piscataway, New Jersey 08854, United States

Wenqian Xu – X-ray Science Division, Advanced Photon Source, Argonne National Laboratory, Lemont, Illinois 60439, United States

Saul H. Lapidus – X-ray Science Division, Advanced Photon Source, Argonne National Laboratory, Lemont, Illinois 60439, United States; orcid.org/0000-0002-7486-4325

Nirmal J. Ghimire – Department of Physics and Astronomy and Quantum Science and Engineering Center, George Mason University, Fairfax, Virginia 22030, United States; orcid.org/0000-0002-8474-4968

Complete contact information is available at:

<https://pubs.acs.org/10.1021/acs.inorgchem.1c02535>

Notes

The authors declare no competing financial interest.

■ ACKNOWLEDGMENTS

C.M.S., X.T., and N.J.G. were supported by the start-up funding from the George Mason University. C.-J.K. was supported by the NRF grant (NRF-2021R1F1A1063691). Use of the Advanced Photon Source at the Argonne National Laboratory was supported by the U.S. Department of Energy, Office of Science, Office of Basic Energy Sciences, under Contract No. DE-AC02-06CH11357. TEM work was performed at the National High Magnetic Field Laboratory, which is supported by the National Science Foundation Cooperative Agreement No. DMR-1644779 and the State of Florida. XANES work used beamline 7-BM (QAS) of the National Synchrotron Light Source II, a U. S. Department of Energy (DOE) Office of Science User Facility operated for DOE Office of Science by Brookhaven National Laboratory under Contract No. DE-SC0012704. The solid-state 500 MHz NMR spectrometer at the University of Maryland (UMD) was supported by the NSF MRI grant (NSF-1726058). The authors thank Dr. David Walker at the Columbia University for helping press the dense pellet.

■ ADDITIONAL NOTE

^aCertain commercial equipment, instruments, or materials are identified in this document. Such identification does not imply recommendation or endorsement by the National Institute of Standards and Technology, nor does it imply that the products identified are necessarily the best available for the purpose.

■ REFERENCES

- (1) Ye, F.; Chi, S.; Cao, H.; Chakoumakos, B. C.; Fernandez-Baca, J. A.; Custelcean, R.; Qi, T. F.; Korneta, O. B.; Cao, G. Direct Evidence of a Zigzag Spin-Chain Structure in the Honeycomb Lattice: A Neutron and x-Ray Diffraction Investigation of Single-Crystal Na_2IrO_3 . *Phys. Rev. B* **2012**, *85*, No. 180403.
- (2) Kim, B. J.; Jin, H.; Moon, S. J.; Kim, J. Y.; Park, B. G.; Leem, C. S.; Yu, J.; Noh, T. W.; Kim, C.; Oh, S. J.; et al. Novel $J_{\text{eff}} = 1/2$ Mott State Induced by Relativistic Spin-Orbit Coupling in Sr_2IrO_4 . *Phys. Rev. Lett.* **2008**, *101*, No. 076402.
- (3) Yang, B. J.; Kim, Y. B. Topological Insulators and Metal-Insulator Transition in the Pyrochlore Iridates. *Phys. Rev. B* **2010**, *82*, No. 085111.
- (4) Lawler, M. J.; Kee, H. Y.; Kim, Y. B.; Vishwanath, A. Topological Spin Liquid on the Hyperkagome Lattice of $\text{Na}_4\text{Ir}_3\text{O}_8$. *Phys. Rev. Lett.* **2008**, *100*, No. 227201.
- (5) Li, L.; Kong, P. P.; Qi, T. F.; Jin, C. Q.; Yuan, S. J.; Delong, L. E.; Schlottmann, P.; Cao, G. Tuning the $J_{\text{eff}} = 1/2$ Insulating State via Electron Doping and Pressure in the Double-Layered Iridate $\text{Sr}_3\text{Ir}_2\text{O}_7$. *Phys. Rev. B* **2013**, *87*, No. 235127.

- (6) Wang, F. A.; Senthil, T. Twisted Hubbard Model for Sr_2IrO_4 : Magnetism and Possible High Temperature Superconductivity. *Phys. Rev. Lett.* **2011**, *106*, No. 136402.
- (7) Korneta, O. B.; Qi, T.; Chikara, S.; Parkin, S.; De Long, L. E.; Schlottmann, P.; Cao, G. Electron-Doped $\text{Sr}_2\text{IrO}_{4-\delta}$ ($0 \leq \delta \leq 0.04$): Evolution of a Disordered $J_{\text{eff}} = 1/2$ Mott Insulator into an Exotic Metallic State. *Phys. Rev. B* **2010**, *82*, No. 115117.
- (8) Cao, G.; Durairaj, V.; Chikara, S.; DeLong, L. E.; Parkin, S.; Schlottmann, P. Non-Fermi-Liquid Behavior in Nearly Ferromagnetic SrIrO_3 Single Crystals. *Phys. Rev. B* **2007**, *76*, No. 100402.
- (9) Maiti, K.; Singh, R. S.; Medicherla, V. R. R.; Rayaprol, S.; Sampathkumaran, E. V. Origin of Charge Density Wave Formation in Insulators from a High Resolution Photoemission Study of BaIrO_3 . *Phys. Rev. Lett.* **2005**, *95*, No. 016404.
- (10) Hou, Y. S.; Xiang, H. J.; Gong, X. G. Unveiling the Origin of the Basal-Plane Antiferromagnetism in the Spin-Orbit Mott Insulator Ba_2IrO_4 : A Density Functional and Model Hamiltonian Study. *New J. Phys.* **2016**, *18*, No. 043007.
- (11) Yang, K.; Lu, Y.; Ran, Y. Quantum Hall Effects in a Weyl Semimetal: Possible Application in Pyrochlore Iridates. *Phys. Rev. B* **2011**, *84*, No. 075129.
- (12) Ueda, K.; Oh, T.; Yang, B. J.; Kaneko, R.; Fujioka, J.; Nagaosa, N.; Tokura, Y. Magnetic-Field Induced Multiple Topological Phases in Pyrochlore Iridates with Mott Criticality. *Nat. Commun.* **2017**, *8*, No. 15515.
- (13) Okamoto, Y.; Nohara, M.; Aruga-Katori, H.; Takagi, H. Spin-Liquid State in the $S = 1/2$ Hyperkagome Antiferromagnet $\text{Na}_4\text{Ir}_3\text{O}_8$. *Phys. Rev. Lett.* **2007**, *99*, No. 137207.
- (14) Gadzhiev, M. I.; Shaplygin, I. S. Lithium Oxide-Iridium Dioxide System. *Zh. Neorg. Khim.* **1984**, *29*, 2155–2156.
- (15) Scholder, R.; Glaeser, H. Lithium and Sodium Uranates(V) and Structural Relations between Compounds of the Type Li_7AO_6 and Li_8AO_6 . *Z. Anorg. Allg. Chem.* **1964**, *327*, 15–27.
- (16) Scholder, R.; Raede, D.; Schwarz, H. Lithium Plumbates(IV) and Stannates(IV). *Z. Anorg. Allg. Chem.* **1969**, *364*, 113–126.
- (17) Shaplygin, I. S.; Gadzhiev, M. I.; Lazarev, V. B. Lithium Oxide-Ruthenium Dioxide System. *Zh. Neorg. Khim.* **1987**, *32*, 746–748.
- (18) Hauck, J. Lithium Hexaoxometallates. *Z. Naturforsch., B* **1969**, *24*, 1067–1068.
- (19) Hofmann, R.; Hoppe, R. A New Oxogermanate: Lithium Germanate Oxide (Li_8GeO_6) = $\text{Li}_8\text{O}_2[\text{GeO}_4]$. *Z. Anorg. Allg. Chem.* **1987**, *555*, 118–128.
- (20) Schartau, W.; Hoppe, R. New Alkali Metal Silicates. *Naturwissenschaften* **1973**, *60*, No. 256.
- (21) Jansen, M.; Hoppe, R. Alkali Metal Oxocobaltates. Lithium Oxocobaltate (Li_8CoO_6). *Z. Anorg. Allg. Chem.* **1973**, *398*, 54–62.
- (22) Mühle, C.; Karpov, A.; Verhoeven, A.; Jansen, M. Crystal Structures, Dimorphism and Lithium Mobility of Li_7MO_6 ($M = \text{Bi}, \text{Ru}, \text{Os}$). *Z. Anorg. Allg. Chem.* **2005**, *631*, 2321–2327.
- (23) Itoh, Y.; Michioka, C.; Yoshimura, K.; Nakajima, K.; Sato, H. Critical Slowing down of Triangular Lattice Spin-3/2 Heisenberg Antiferromagnet Li_7RuO_6 via ^7Li NMR. *J. Phys. Soc. Jpn.* **2009**, *78*, No. 023705.
- (24) Huang, S.; Wilson, B. E.; Wang, B.; Fang, Y.; Buffington, K.; Stein, A.; Truhlar, D. G. Y-Doped Li_xZrO_6 : A Li-Ion Battery Cathode Material with High Capacity. *J. Am. Chem. Soc.* **2015**, *137*, 10992–11003.
- (25) Luo, N.; Hou, Z.; Zheng, C.; Zhang, Y.; Stein, A.; Huang, S.; Truhlar, D. G. Anionic Oxygen Redox in the High-Lithium Material Li_8SnO_6 . *Chem. Mater.* **2021**, *33*, 834–844.
- (26) Kirklin, S.; Chan, M. K. Y.; Trahey, L.; Thackeray, M. M.; Wolverton, C. High-Throughput Screening of High-Capacity Electrodes for Hybrid Li-Ion-Li-O₂ Cells. *Phys. Chem. Chem. Phys.* **2014**, *16*, 22073–22082.
- (27) Brice, J.-F.; Ramdani, A. Electrical Conductivity of Lithium Cerium Oxide (Li_8CeO_6) and Lithium Hafnium Oxide (Li_8HfO_6). *Mater. Res. Bull.* **1981**, *16*, 1487–1492.
- (28) Cova, F.; Amica, G.; Kohopää, K.; Blanco, M. V. Time-Resolved Synchrotron Powder X-Ray Diffraction Studies on the Synthesis of Li_8SiO_6 and Its Reaction with CO_2 . *Inorg. Chem.* **2019**, *58*, 1040–1047.
- (29) Rodríguez-Carvajal, J. Recent Advances in Magnetic Structure Determination by Neutron Powder Diffraction. *Phys. B* **1993**, *192*, 55–69.
- (30) Blaha, P.; Schwarz, K.; Tran, F.; Laskowski, R.; Madsen, G. K. H.; Marks, L. D. WIEN2k: An APW+lo Program for Calculating the Properties of Solids. *J. Chem. Phys.* **2020**, *152*, No. 074101.
- (31) Georges, A.; Kotliar, G.; Krauth, W.; Rozenberg, M. J. Dynamical Mean-Field Theory of Strongly Correlated Fermion Systems and the Limit of Infinite Dimensions. *Rev. Mod. Phys.* **1996**, *68*, 13–123.
- (32) Kotliar, G.; Savrasov, S. Y.; Haule, K.; Oudovenko, V. S.; Parcollet, O.; Marianetti, C. A. Electronic Structure Calculations with Dynamical Mean-Field Theory. *Rev. Mod. Phys.* **2006**, *78*, 865–951.
- (33) Haule, K.; Yee, C. H.; Kim, K. Dynamical Mean-Field Theory within the Full-Potential Methods: Electronic Structure of CeIrIn_5 , CeCoIn_5 , and CeRhIn_5 . *Phys. Rev. B* **2010**, *81*, No. 195107.
- (34) Werner, P.; Comanac, A.; De Medici, L.; Troyer, M.; Millis, A. J. Continuous-Time Solver for Quantum Impurity Models. *Phys. Rev. Lett.* **2006**, *97*, No. 076405.
- (35) Haule, K. Quantum Monte Carlo Impurity Solver for Cluster Dynamical Mean-Field Theory and Electronic Structure Calculations with Adjustable Cluster Base. *Phys. Rev. B* **2007**, *75*, No. 155113.
- (36) Zhang, H.; Haule, K.; Vanderbilt, D. Effective $J = 1/2$ Insulating State in Ruddlesden-Popper Iridates: An LDA+DMFT Study. *Phys. Rev. Lett.* **2013**, *111*, No. 246402.
- (37) Zhang, H.; Haule, K.; Vanderbilt, D. Metal-Insulator Transition and Topological Properties of Pyrochlore Iridates. *Phys. Rev. Lett.* **2017**, *118*, No. 026404.
- (38) Feng, H. L.; Kang, C. J.; Deng, Z.; Croft, M.; Liu, S.; Tyson, T. A.; Lapidus, S. H.; Frank, C. E.; Shi, Y.; Jin, C.; et al. $\text{Ti}_2\text{Ir}_2\text{O}_7$: A Pauli Paramagnetic Metal, Proximal to a Metal Insulator Transition. *Inorg. Chem.* **2021**, *60*, 4424–4433.
- (39) Jarrell, M.; Gubernatis, J. E. Bayesian Inference and the Analytic Continuation of Imaginary-Time Quantum Monte Carlo Data. *Phys. Rep.* **1996**, *269*, 133–195.
- (40) Kroeschell, P.; Wolf, R.; Hoppe, R. New Compounds of the Lithium Tin Oxide (Li_8SnO_6)-Type: Lithium Iridium Oxide (Li_8IrO_6), Lithium Platinum Oxide (Li_8PtO_6), and Lithium Cerium Oxide (Li_8CeO_6). *Z. Anorg. Allg. Chem.* **1986**, *536*, 81–91.
- (41) Singh, Y.; Manni, S.; Reuther, J.; Berlijn, T.; Thomale, R.; Ku, W.; Trebst, S.; Gegenwart, P. Relevance of the Heisenberg-Kitaev Model for the Honeycomb Lattice Iridates A_2IrO_3 . *Phys. Rev. Lett.* **2012**, *108*, No. 127203.
- (42) Singh, Y.; Gegenwart, P. Antiferromagnetic Mott Insulating State in Single Crystals of the Honeycomb Lattice Material Na_2IrO_3 . *Phys. Rev. B* **2010**, *82*, No. 064412.
- (43) Mühle, C.; Dinnebier, R. E.; Van Wullen, L.; Schwering, G.; Jansen, M. New Insights into the Structural and Dynamical Features of Lithium Hexaoxometallates Li_7MO_6 ($M = \text{Nb}, \text{Ta}, \text{Sb}, \text{Bi}$). *Inorg. Chem.* **2004**, *43*, 874–881.
- (44) O'Malley, M. J.; Verweij, H.; Woodward, P. M. Structure and Properties of Ordered Li_2IrO_3 and Li_2PtO_3 . *J. Solid State Chem.* **2008**, *181*, 1803–1809.
- (45) Altermatt, D.; Brown, I. D. The Automatic Searching for Chemical Bonds in Inorganic Crystal Structures. *Acta Crystallogr., Sect. B: Struct. Sci.* **1985**, *41*, 240–244.
- (46) Xu, Z.; Stebbins, J. F. ^6Li Nuclear Magnetic Resonance Chemical Shifts, Coordination Number and Relaxation in Crystalline and Glassy Silicates. *Solid State Nucl. Magn. Reson.* **1995**, *5*, 103–112.
- (47) Popov, G.; Greenblatt, M.; Croft, M. Large Effects of A-Site Average Cation Size on the Properties of the Double Perovskites $\text{Ba}_{2-x}\text{Sr}_x\text{MnReO}_6$: A $d^5 - d^1$ System. *Phys. Rev. B* **2003**, *67*, No. 024406.
- (48) Mandal, T. K.; Poltavets, V. V.; Croft, M.; Greenblatt, M. Synthesis, Structure and Magnetic Properties of $\text{A}_2\text{MnB}'\text{O}_6$ ($A = \text{Ca}, \text{Sr}; B' = \text{Sb}, \text{Ta}$) Double Perovskites. *J. Solid State Chem.* **2008**, *181*, 2325–2331.

(49) Retuerto, M.; Li, M. R.; Stephens, P. W.; Sánchez-Benítez, J.; Deng, X.; Kotliar, G.; Croft, M. C.; Ignatov, A.; Walker, D.; Greenblatt, M. Half-Metallicity in $\text{Pb}_2\text{CoReO}_6$ Double Perovskite and High Magnetic Ordering Temperature in $\text{Pb}_2\text{CrReO}_6$ Perovskite. *Chem. Mater.* **2015**, *27*, 4450–4458.

(50) Feng, H. L.; Deng, Z.; Wu, M.; Croft, M.; Lapidus, S. H.; Liu, S.; Tyson, T. A.; Ravel, B. D.; Quackenbush, N. F.; Frank, C. E.; et al. High-Pressure Synthesis of $\text{Lu}_2\text{NiIrO}_6$ with Ferrimagnetism and Large Coercivity. *Inorg. Chem.* **2019**, *58*, 397–404.

(51) Frank, C. E.; McCabe, E. E.; Orlandi, F.; Manuel, P.; Tan, X.; Deng, Z.; Croft, M.; Cascos, V.; Emge, T.; Feng, H. L.; et al. $\text{Mn}_2\text{CoReO}_6$ a Robust Multisublattice Antiferromagnetic Perovskite with Small A-Site Cations. *Chem. Commun.* **2019**, *55*, 3331–3334.

(52) Li, M. R.; Croft, M.; Stephens, P. W.; Ye, M.; Vanderbilt, D.; Retuerto, M.; Deng, Z.; Grams, C. P.; Hemberger, J.; Hadermann, J.; et al. Mn_2FeWO_6 : A New Ni_3TeO_6 -Type Polar and Magnetic Oxide. *Adv. Mater.* **2015**, *27*, 2177–2181.

(53) Feng, H. L.; Deng, Z.; Segre, C. U.; Croft, M.; Lapidus, S. H.; Frank, C. E.; Shi, Y.; Jin, C.; Walker, D.; Greenblatt, M. High-Pressure Synthesis of Double Perovskite $\text{Ba}_2\text{NiIrO}_6$: In Search of a Ferromagnetic Insulator. *Inorg. Chem.* **2021**, *60*, 1241–1247.

(54) Laguna-Marco, M. A.; Kayser, P.; Alonso, J. A.; Martínez-Lope, M. J.; Van Veenendaal, M.; Choi, Y.; Haskel, D. Electronic Structure, Local Magnetism, and Spin-Orbit Effects of Ir(IV)-, Ir(V)-, and Ir(VI)-Based Compounds. *Phys. Rev. B* **2015**, *91*, No. 214433.

(55) Nakajima, K.; Sato, H.; Fukui, T.; Iwaki, M.; Narumi, Y.; Kindo, K.; Itoh, Y.; Michioka, C.; Yoshimura, K. Li_7RuO_6 : As a 4d Heisenberg Frustrated Magnet. *J. Phys. Soc. Jpn.* **2010**, *79*, No. 064705.

(56) Cao, G.; Bolivar, J.; McCall, S.; Crow, J.; Guertin, R. Weak Ferromagnetism, Metal-to-Nonmetal Transition, and Negative Differential Resistivity in Single-Crystal Sr_2IrO_4 . *Phys. Rev. B* **1998**, *57*, R11039–R11042.

(57) Isobe, M.; Okabe, H.; Akimitsu, J. Magnetic States in Quasi-2-D Iridium Oxides with Large Spin-Orbit Coupling. *J. Korean Phys. Soc.* **2013**, *63*, 394–397.

(58) Shapiro, M. C.; Riggs, S. C.; Stone, M. B.; De La Cruz, C. R.; Chi, S.; Podlesnyak, A. A.; Fisher, I. R. Structure and Magnetic Properties of the Pyrochlore Iridate $\text{Y}_2\text{Ir}_2\text{O}_7$. *Phys. Rev. B - Condens. Matter Mater. Phys.* **2012**, *85*, 214434.

(59) Dhital, C.; Khadka, S.; Yamani, Z.; De La Cruz, C.; Hogan, T. C.; Disseler, S. M.; Pokharel, M.; Lukas, K. C.; Tian, W.; Opeil, C. P.; et al. Spin Ordering and Electronic Texture in the Bilayer Iridate $\text{Sr}_3\text{Ir}_2\text{O}_7$. *Phys. Rev. B - Condens. Matter Mater. Phys.* **2012**, *86*, No. 100401.

(60) Abramchuk, M.; Ozsoy-Keskinbora, C.; Krizan, J. W.; Metz, K. R.; Bell, D. C.; Tafti, F. Cu_2IrO_3 : A New Magnetically Frustrated Honeycomb Iridate. *J. Am. Chem. Soc.* **2017**, *139*, 15371–15376.

(61) Ma, H. J. H.; Yang, P.; Lim, Z. S.; et al. Ariando. Mott Variable Range Hopping and Bad-Metal in Lightly Doped Spin-Orbit Mott Insulator BaIrO_3 . *Phys. Rev. Mater.* **2018**, *2*, No. 065003.

(62) Sala, M. M.; Ohgushi, K.; Al-Zein, A.; Hirata, Y.; Monaco, G.; Krisch, M. CaIrO_3 : A Spin-Orbit Mott Insulator beyond the $J_{\text{eff}} = 1/2$ Ground State. *Phys. Rev. Lett.* **2014**, *112*, No. 176402.

(63) Kim, H. J.; Lee, J. H.; Cho, J. H. Antiferromagnetic Slater Insulator Phase of Na_2IrO_3 . *Sci. Rep.* **2015**, *4*, No. 5253.

(64) Arita, R.; Kune, J.; Kozhevnikov, A. V.; Eguluz, A. G.; Imada, M. Ab Initio Studies on the Interplay between Spin-Orbit Interaction and Coulomb Correlation in Sr_2IrO_4 and Ba_2IrO_4 . *Phys. Rev. Lett.* **2012**, *108*, No. 086403.